Catena 187 (2020) 104373

Contents lists available at ScienceDirect

Catena

journal homepage: www.elsevier.com/locate/catena

Does edge erosion alter coastal wetland soil properties? A multi-method biogeochemical study

Havalend E. Steinmuller[a], Michael P. Hayes[b], Nia R. Hurst[a,c], Yadav Sapkota[d], Robert L. Cook[b,*], John R. White[d,*], Zuo Xue[d], Lisa G. Chambers[a,*]

[a] Aquatic Biogeochemistry Laboratory, Department of Biology, University of Central Florida, Orlando, FL, USA
[b] Department of Chemistry, Louisiana State University, Baton Rouge, LA, USA
[c] Engineer Research and Development Center, US Army Corps of Engineers, Vicksburg, MS, USA
[d] Department of Oceanography and Coastal Sciences, Louisiana State University, Baton Rouge, LA, USA

ARTICLE INFO

Keywords:
Carbon mineralization
Marsh edge
Saltwater incursion
Coastal marsh loss
Spectroscopic indicators

ABSTRACT

Coastal wetlands in Louisiana experience high rates of edge erosion due to combined eustatic sea level rise and coastal subsidence. This study sought to (1) evaluate site-specific spatial and temporal patterns in marsh edge erosion rates within Barataria Bay, LA, (2) develop an understanding of the physical and chemical properties of eroding soils through biogeochemical and spectroscopic characterization, and (3) evaluate interactions between erosion, saltwater incursion, and soil properties through a comparison of sites with different erosion rates and varying distances from the eroding edge. Replicate soil cores were collected at three distances inland (1 m, 3 m, 5 m) at three different sites (west, south, and north) to a depth of 1 m. Erosion rates were measured at each site, and soils were sectioned into 10 cm intervals for a total of 270 soil and porewater samples. Each soil sample was subjected to soil physicochemical analysis (bulk density, moisture content, organic matter content, and total carbon (C), nitrogen (N), and phosphorus (P)) as well as assessments of biogeochemical cycling (production of CO_2, mineralization of N and P, and extractable nutrient concentrations). Porewater samples were analyzed to elucidate spectroscopic and fluorometric indicators of carbon quality (aromaticity, humification, lignin proportion, and C source). Erosion rates at the west, north, and south sites were 3.36 ± 0.4, 1.34 ± 0.2, and 0.58 ± 0.03 m yr^{-1}, respectively. Neither erosional magnitude nor saltwater incursion was found to be significant predictors of any measured spectroscopic or biogeochemical parameters, though depth was a significant control on 18 of the measured 20 parameters. The top 30 cm were more biologically active (as indicated by greater mineralization of C, N and P) and were characterized by lower molecular weight porewater DOM with less aromaticity. Degree of humification and aromaticity of porewater DOM increased with both depth and distance inland. Concentrations of bioavailable N and P at 1 m depth were at least 5 times greater than surface concentrations, representing a pool of nutrients that could be exported into the coastal ocean with ongoing erosion. This study is the first to couple spectroscopic and biogeochemical measurements for the purpose of assessing soil and porewater physicochemistry within wetland soils and illustrates an as-yet unaccounted for potential for the export of labile C, N, and P into the coastal ocean.

1. Introduction

Coastal wetlands experience both direct effects of sea level rise (increases in inundation and salinity) and indirect effects (increases in marsh edge erosion). Marsh edge erosion is a process facilitated by greater wave height, tidal amplitude, and tidal duration and is exacerbated by an insufficient sediment supply, resulting in the loss of physical components of the marsh platform due to wave action. This pattern of edge erosion has been observed to varying degrees on wetland-dominated coastlines globally (DeLaune and White, 2012; Morton et al., 2009; Sapkota and White, 2019a,b). Coastal marshes with large adjacent bays and shallow topography are especially vulnerable to erosional processes. Shallow topography can promote an increase in wave height, while large areas of open water contribute to a greater wind fetch, further increasing wave energy (Leonardi et al., 2016b; Munk and Traylor, 1947). These processes work synergistically with other ecogeomorphic landscape components to increase erosional magnitude along the marsh edge, physically scouring-out light fractions

* Corresponding authors.
E-mail addresses: rlcook@lsu.edu (R.L. Cook), jrwhite@lsu.edu (J.R. White), lisa.chambers@ucf.edu (L.G. Chambers).

https://doi.org/10.1016/j.catena.2019.104373
Received 29 August 2019; Received in revised form 11 November 2019; Accepted 14 November 2019

of the soil matrix from the interface of the aquatic edge (McLoughlin et al., 2015). Eventually, the loss of soil particles from the marsh edge results in 'mass failure', where large blocks of heavily rooted surface soils break off from the edge and are disarticulated within the adjacent water body (Francalanci et al., 2013).

Previous studies have demonstrated that the effects of erosion are mediated by both extrinsic (ecogeomorphological) and intrinsic (characteristics of the marsh) properties (Wang et al., 2017). In terms of extrinsic factors, erosion magnitude has been shown to depend on wind-driven waves, long-shore currents, tidal regimes, fetch, and the area and bathymetry of the adjacent bay (Hu et al., 2015; Koppel et al., 2004; Manca et al., 2012; Möller et al., 2014; Sapkota and White, 2019a,b; Schwimmer, 2001; Wang et al., 2017; Yang et al., 2012). Conversely, the intrinsic characteristics that regulate erosion have received less attention. Through a series of experimental manipulations, Feagin et al. (2009) demonstrated that soil type (i.e. particle size), rather than vegetation, was the primary mediator of lateral erosional magnitude within coastal marshes. Similarly, Sapkota and White (2019a,b) illustrated correlations between erosion rate and soil physicochemical properties. Generally, these studies have focused on the physical effects of marsh edge erosion on the soil structure and have largely disregarded the chemical effects. Within salt and brackish ecosystems, the seawater eroding the marsh structure is characterized by both high ionic strength and high sulfate concentrations, an alternative terminal electron acceptor, for respiration within soil microorganisms (Reddy and DeLaune, 2008). Combined with the physical dynamics of flushing driven by wave action and tidal inundation cycles, it is reasonable to assume that this high salinity seawater can infiltrate the porespaces within the soil matrix along the eroding edge. Effectively acting as saltwater incursion, this infiltration could disrupt biogeochemical cycling within the soil matrix by liberating bioavailable nutrients (Steinmuller and Chambers, 2018), providing an alternative electron acceptor to increase carbon dioxide production (Chambers et al., 2013, 2011), altering the microbial community composition (Herbert et al., 2015), and/or contributing to flocculation of dissolved organic carbon (DOC) (Ardón et al., 2016). These processes, especially the enhancement of C mineralization, have the potential to weaken the soil structure, further facilitating erosion and thereby creating a positive feedback loop that has not been investigated or accounted for within erosion models. As a result, this study sought to fill this knowledge gap through a novel analysis: coupling biogeochemical and spectroscopic analyses to determine if soil loss and subsurface incursion of bay water into the marsh platform near the eroding edge can physically and/or chemically alter soil and porewater properties in advance of soil collapse, potentially creating a feedback mechanism that promotes marsh loss.

Spectroscopic assessment of porewater dissolved organic material (DOM) utilizes both ultraviolet (UV)/visible (vis) and fluorometric intensities to provide information on present C moieties. More specifically, these analyses can offer insight into the molecular complexity, degree of decomposition, and source (biological vs. terrestrial) of DOM (Table 1; Haywood et al., 2018). Previously, these indicators have been used to characterize quinones in DOM, water pollution levels, the biodegradability of forest soils, and DOM transformations (Cook et al., 2009; Cory and McKnight, 2005; Fellman et al., 2010; Haywood et al., 2018; Hudson et al., 2007; Wang et al., 2013). These spectroscopic analyses, coupled with measurements of soil physicochemical properties and microbially-mediated biogeochemical transformations, represent the first assessment of both chemical and physical effects of erosion. The overall goals of this study were to, (1) evaluate site-specific spatial and temporal patterns in erosion rate/wetland loss, (2) develop a comprehensive understanding of the physical and chemical properties of the soils undergoing erosion through coupled biogeochemical and spectroscopic characterization, and (3) evaluate potential interactions

Table 1
Spectroscopic and biogeochemical analyses, separated by matrix, chemical/biological/physical meaning, and ecological indicator. (Cation exchange complex is denoted as CEC., PW denotes 'porewater'.). Adapted from Kolic et al. (2014).

Measurement	Matrix	Chemical/biological/physical meaning	Ecological indication
Soil physicochemical characteristics			
Bulk density	Soil	Weight of soil within a given volume	Soil type
Moisture content	Soil	Determination of the % of the bulk soil that is water	Soil type
OM	Soil (Dried)	Fraction of bulk soil that is organic material	Soil type
TP	Soil (Dried)	P content within bulk soil	Supports biogeochemical cycling of P
TN	Soil (Dried)	N content within bulk soil	Supports biogeochemical cycling of N
TC	Soil (Dried)	C content within bulk soil	Supports biogeochemical cycling
Salinity/conductivity	PW	Conductivity of soil porewater	Measurement of physicochemical environment
Nutrient availability			
Ext. NO_3^-	Soil + PW	NO_3^- within both the porewater and/or adhered to the CEC	Inorganic N to support biological processes
Ext. SRP	Soil + PW	SRP within both the porewater and/or adhered to the CEC	Organic P to support biological processes
Ext. NH_4^+	Soil + PW	NH_4^+ within both the porewater and/or adhered to the CEC	Inorganic N to support biological processes
Microbially-mediated biogeochemical transformations			
CO_2 production	Soil + PW	Potential CO_2 emitted from microbial respiration as a rate	Mineralization of C by resident soil microbes
CH_4 production	Soil + PW	Potential CH_4 emitted from methanogenesis as a rate	Mineralization of C through methanogenesis
PMN rate	Soil + PW	Potential NH_4^+ mineralized by microbial consortia over time	Mineralization of organic matter to liberate inorganic N
PMP rate	Soil + PW	Potential SRP mineralized by microbial consortia over time	Mineralization of organic matter to liberate organic P
UV–visible indicators			
A_{254}	PW	Amount of DOM aromatic moieties	Plant inputs, degradation pathways, refractory DOM
A_{350}	PW	Amount of DOM lignin moieties	Plant and terrestrial DOM inputs
S_{275}	PW	Indicator of lignin molecular weight	Indicator of degree of degradation of DOM
Spectroscopic analyses			
FI	PW	Autochthonous vs. allochthonous production of DOM	Degree of terrestrial nature of DOM
BIX	PW	Fresh protein inputs within DOM pool	Assessment of 'freshness' of biological activity within DOM
HIX	PW	Red shifting of fluorophores	Extent of humification of DOM
PARAFACs components			
Fluorophore A	PW	Combination of UV humic-like and aquatic-like material	Indicator of aquatic-like sourced, recently produced material
Fluorophore B	PW	Protein-like DOM in system	Indicator of biologically-sourced material
Fluorophore T	PW	Combination of Vis humic-like and soil fulvic acid material	Indicator of terrestrial-like sourced, older material

between erosion, saltwater incursion, and soil properties by comparing sites with varying erosion rates (represented by direction) and distance from the eroding edge.

2. Methods

2.1. Site description and erosional measurements

The study was conducted on a newly formed island, recently eroded from a larger, contiguous coastal marsh within northern Barataria Bay, LA (USA, Fig. 1). Barataria Bay, LA is experiencing land loss rates of 13.33 km^2 yr^{-1} (Couvillion et al. 2017), caused by high rates of edge erosion (1.41 m yr^{-1}). The island used for this study (1068 m^2 area) was dominated by *Spartina alterniflora*, with a patch of *Iva frutescens* near the center of the island (Fig. 2). This region of Barataria Bay is considered microtidal with diurnal inundation (Georgiou et al., 2005). The salinity typically ranges from 10 to 25 ppt (White et al., 2018) and the edge of the marsh platform was characterized by a scarp approximately 36 cm high (Sapkota and White, 2019a,b) that separates the island from the surrounding shallow bay. This location was selected due to varying erosion rates and range of cardinal direction.

Three erosion measurement transects were established at each of three direction in February 2018 (Fig. 2). Each transect consisted of three PVC poles (2.5 m long) installed at 1 m intervals starting 1 m from the current marsh edge. The distance between the marsh edge and the nearest pole was recorded at least once every two months. As erosion proceeded to remove the most seaward pole, inland replacements were added at 1 m intervals to maintain transects of three poles. Historical erosion rates were obtained from Google Earth imagery. The distance from the current position of the marsh edge to the historical edges in 1998, 2005, 2012, and 2016 were measured for each transect using the time series of Google Earth images to calculate longer-term erosion rates.

2.2. Soil and water sampling

Duplicate 1 m deep soil cores were collected 1 m from the established erosion transects (west, north, and south) at intervals of 1 m, 3 m, and 5 m inland from the marsh edge. Soil cores were collected on July 16, 2018 (west and south) and August 2, 2018 (north). A polycarbonate core tube (1.7 m × 7.6 cm diameter) was used to extract soil samples via the push core method. Soils were extruded in the field into 10 separate 10-cm intervals and placed in sealed polyethylene bags. Samples were stored on ice, promptly transported to Louisiana State University (LSU), and stored at 4 °C until processing.

Ambient salinity, temperature, and dissolved oxygen concentrations were determined at each sampling site by use of a sonde (YSI Inc., Yellow Spring, OH) in the field. Three (3) L of surface water was collected into polyethylene bottles and vacuum-filtered through Supor 0.45 μm membrane filters. Following filtration, water samples were stored on ice and transported back to the University of Central Florida (UCF) for further processing.

2.3. Sample processing

Each 10-cm soil sample was initially weighed, homogenized, and separated into three subsamples for analysis: one used for determination of soil moisture content, bulk density, percent organic matter

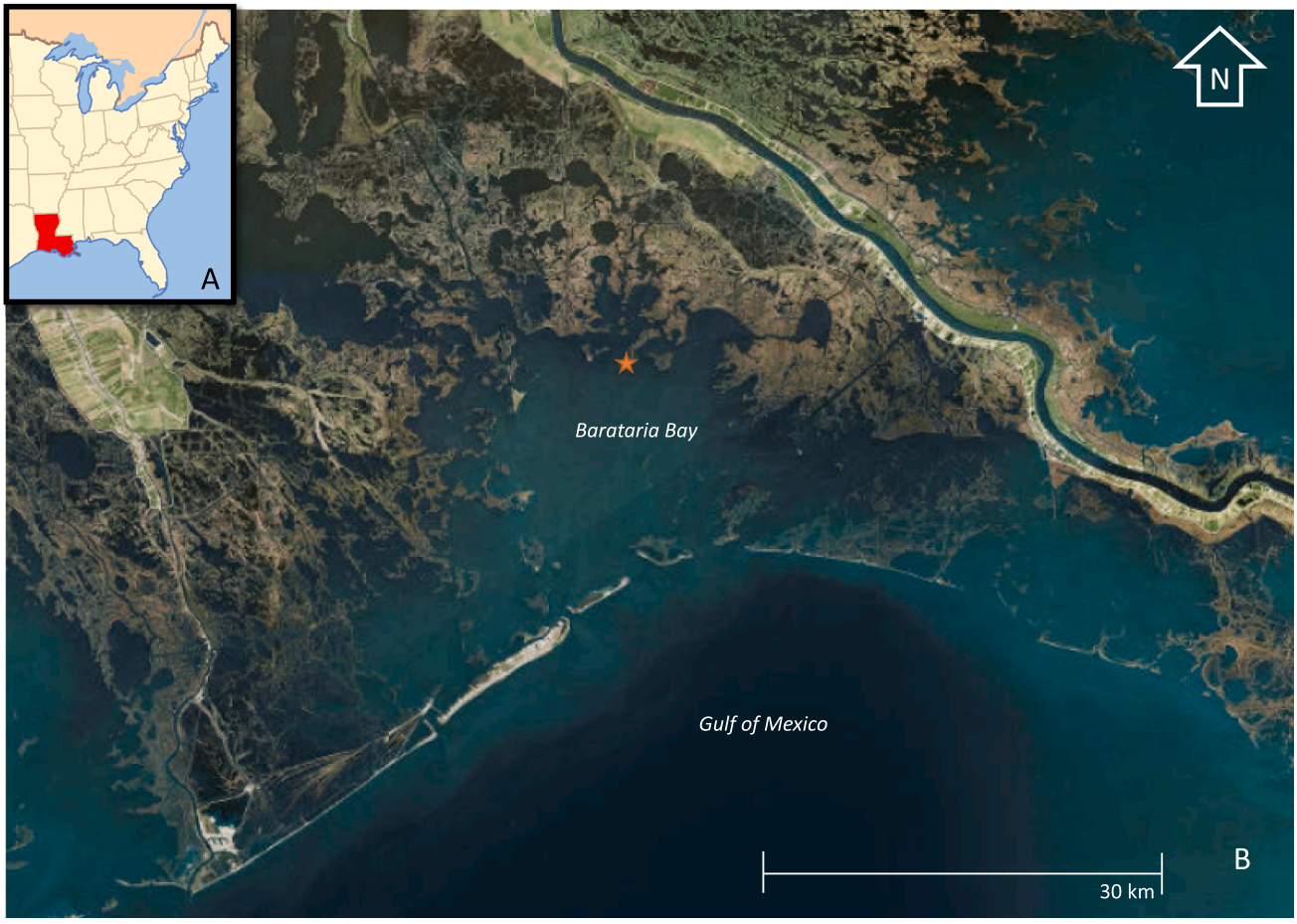

Fig. 1. Location of Louisiana within the Eastern United States (A) and Barataria Bay, LA (B). Star indicates site location. (Google Earth Pro version 7.3.2.5776.) Coordinates of star/site are 29°26′39.60″N, 89°53′59.12″W.

Fig. 2. Map of locations of erosion transects, where triangles indicate locations of the North transects, circles denote West transects, and squares denote South. Sampling locations were located adjacent to erosion transects. Image courtesy of Eddie Weeks.

(OM), total soil carbon (TC), nitrogen (TN), and phosphorus (TP); one for determination spectroscopic indicators, including UV–Vis indices (absorbance at 254 nm; A_{254}, absorbance at 350 nm; A_{350}, and spectral slope; S_{275}) and fluorescence indices (fluorescence index; FI, biological index; BIX, and humification index; HIX); and one for determination of soil greenhouse gas (carbon dioxide (CO_2) and methane (CH_4)) production, soil pH, and extractable nutrients (ammonium (NH_4^+), nitrate (NO_3^-), and soluble reactive phosphorus (SRP)), and potentially mineralizable N and P.

2.3.1. Soil physicochemical characteristics

Soil samples (n = 270) were analyzed for moisture content, bulk density, OM, TC, TN, TP, soil porewater conductivity, and soil pH. Gravimetric moisture content was determined by weighing a 20–30 g subsample of soil before and after drying at 60 °C in a gravimetric oven until a constant mass was achieved. The bulk density of each sample was determined by calculating the total dry mass of the sample divided by the volume of the 10 cm section of the core (384.85 cm^3). The dried samples were ground into fine particles using a mortar and pestle. Total C and TN were determined on the ground subsample using an elemental combustion system (Costech Analytical Technologies, Valencia, CA). Organic matter content was determined by the loss on ignition (LOI) technique, where 0.2–0.5 g samples were weighed in 50 mL glass beakers and ashed in a muffle furnace at 550 °C for 4 hr; percent OM was calculated by dividing the ashed mass of the sample by the pre-ashed mass. Total P was determined by digesting the ashed samples following Andersen et al. (1976) and analyzed colorimetrically using a SEAL AQ2 Automated Discrete Analyzer (SEAL Analytical Inc, Mequon, Wisconsin, EPA method 119-A Rev. 4). Soil pH was measured using a 1:5 slurry of field moist soil and ultrapure water and subsequently measuring pH using an Accumet pH probe (Accumet XL 200, ThermoFisher Scientific, Waltham, MA, USA). Subsamples of field-moist soil were centrifuged at 5000 rpm for 10 min to separate the soil and porewater, following which porewater was decanted and conductivity was measured using a dual channel pH/Ion meter (Fisher Scientific, Hampton, NH). Porewater salinity was then calculated from conductivity and temperature.

2.3.2. Spectroscopic measurements

The soil porewater (collected by centrifuging and decanting each depth increment as mentioned above) was then filtered (0.45 μm × 13 mm Nylon syringe filter) into 20 mL borosilicate glass scintillation vials with poly-seal caps. Samples were diluted by a factor of 2 with ultrapure water (Modulab Water Systems, Lowell, MA). A Cary 100 Spectrophotometer (Varian Inc., Palo Alto, CA) provided UV–Vis absorbance spectra collected from wavelengths of 200 to 600 nm using a 1 nm bandpass with a 1 cm quartz cell (Haywood et al., 2019). The absorbance spectra data yielded three major indicators: A_{254}, A_{350}, and S_{275}. For the spectral slope from 275 to 295 nm (S_{275}), the absorption data was converted to Napierian absorption coefficient, (m^{-1}). Spectral slope coefficients were estimated using a linear fit of the log-linearized spectrum over their respective spectral range and are reported with units of nm^{-1} (Haywood et al., 2018; Kolic et al., 2014).

The filtered porewater from the centrifuged samples was also used

to determine fluorescence indicators. Fluorescence excitation emission matrix spectra (EMMs) were collected on a Spex Fluorolog-3 spectrofluorometer (HORIBA Scientific, Edison, NJ) using a 1 cm quartz cell with emission wavelengths of 250–600 nm and excitation wavelengths of 250–550 nm with 5 nm increments. The Spex Fluorolog-3 uses a 2.0 nm slit width and a 0.5 nm bandpass filter. Along with sample EEMs, blank EEMs of Milli-Q water were collected daily to standardize data. Prior to use for calculation of fluorescence indicators and PARAFAC modeling, the raw fluorescence EEMs for samples and blanks were pre-processed following procedures outlined in Murphy et al. (2010) and Haywood et al. (2018). The pre-processed EEMs were used to calculate the fluorescence indicators used to determine several characteristics of the DOM. Specifically, fluorescence index (FI) was determined by dividing the emission intensity 450 nm (biological) by the 500 nm intensity (terrestrial) at the 370 nm excitation level. The biological index (BIX) was determined by dividing the emission intensity of 380 nm (protein) with the intensity 430 nm (biological) at the excitation wavelength 310 nm. The humification index (HIX) was calculated as the sum of intensities 435–480 nm divided by the sum of 300–345 nm. This number was then added to the sum of 435–480 nm, all at the excitation wavelength of 254 nm (Haywood et al. 2018). PARAFAC analysis followed the procedure outlined by Murphy et al. (2010) and Haywood et al. (2018) and obtained fluorophore components were verified by comparison on OpenChrom (Table 5) with the 3-component model being validated using MATLAB software with multiple validation techniques: split half analysis, visual leverage plot comparison, and core consistency

2.3.3. Greenhouse gas production

Carbon dioxide and CH_4 production were determined by weighing 7 g of field-moist soil into 100 mL glass serum bottles. Bottles were capped with rubber septa and aluminum crimp cap, evacuated to −75 mm Hg, and purged with 99% O_2-free N_2 gas for 3 min. Ten (10) mL of N_2-purged site water was added to the bottles to create a soil slurry and preserve anaerobic conditions. Bottles were placed on an orbital shaker in the dark at 150 rpm and 25 °C. To determine rates of CO_2 and CH_4 production, gas samples were extracted from the headspace of each bottle at 24, 48, 72, and 120 h after addition of site water and injected into a GC-2014 gas chromatograph equipped with a flame ionization detector and methanizer (Shimadzu Instruments, Kyoto, Japan). Production rates were calculated as the change in either CO_2 or CH_4 production over time using Henry's Law and the ideal gas law to account for gas dissolved in the liquid phase, and the influence of pressure and temperature on solubility, respectively (Weiss, 1974).

2.3.4. Extractable nutrients and rates of potential mineralization

Approximately 2.5 g field-moist soil was weighed into 40 mL centrifuge tubes to determine concentrations of extractable NH_4^+, NO_3^-, and SRP. Twenty-five (25) mL of 2 M KCl was added to each tube and samples were shaken continuously on an orbital shaker at 150 rpm and 25 °C for 1 h. Samples were then centrifuged at 4000 rpm for 10 min 10 °C; the supernatant was subsequently vacuum-filtered through Supor 0.4 μm membrane filters and acidified to a pH of < 2 with double-distilled sulfuric acid and stored at 4 °C. Within 25 days, each sample was analyzed for NH_4^+ (US EPA method 350.1, Rev 2.0, 1993), NO_3^- (US EPA method 353.2, Rev 2.0, 1993), and SRP (USEPA method 365.1, Rev. 2.0) colorimetrically via use of a SEAL AQ2 Automated Discrete Analyzer (Seal Analytical, Mequon, WI).

Extractable NH_4^+ and SRP concentrations also represent an initial concentration of bioavailable N and P within each sample (White and Reddy, 2000). Following the bottle incubations for determination of greenhouse gas production, extractions and colorimetric determinations were performed again on the soils within the incubations to provide a second concentration of bioavailable N and P. Rates of potentially mineralizable N and P were determined from the difference between the final and the initial concentration of the nutrient, divided by 7 days.

2.4. Statistical analysis

Statistical analyses were performed using R in RStudio (R Foundation for Statistical Computing, Vienna, Austria; RStudio Inc., Boston, MA, USA), parallel factor analysis (PARAFAC) in MatLab R2016a (Math Works, Inc., Cambridge, MA), and principle component analysis (PCA) in JMP (SAS Institute, Cary, NC). The Shapiro-Wilk test was used to test for normality within each parameter; those that did not meet the assumptions of normality were transformed using a logarithmic transformation for the linear model. Levene's test was then used to determine homogeneity of variance. To determine the interactive effects of direction (a proxy for erosional magnitude, hereafter referred

Table 2
p-values for each fixed effect and each measured parameter, derived from the linear model. Model included depth, direction, and the interaction (fixed effect) as well as transect (random effect). Values in bold are significant (alpha value = 0.003). 'Ext.' refers to extractable.

	Depth	Site	Distance	Depth * site	Depth * distance	Site * distance	Depth * site * distance
Bulk Density	< **0.0001**	0.6507	0.0073	**0.0004**	0.1508	0.1256	0.0080
Moisture content	< **0.0001**	0.1208	0.3575	0.1673	0.0036	0.1336	0.0146
Organic matter	< **0.0001**	0.1484	0.1073	0.6333	**0.0001**	0.4349	0.2117
Total C	< **0.0001**	0.1153	0.919	0.3004	0.6081	0.4280	0.1177
Total N	< **0.0001**	0.0862	0.9987	0.1268	0.5154	0.1002	0.2007
Total P	< **0.0001**	0.0124	< **0.0001**	**0.0023**	**0.0009**	0.1474	0.1790
Salinity	< **0.0001**	< **0.0001**	< **0.0001**	**0.0002**	0.7117	0.5115	0.7408
A254	< **0.0001**	< **0.0001**	< **0.0001**	< **0.0001**	0.0522	< **0.0001**	0.5715
A350	< **0.0001**	**0.0022**	< **0.0001**	< **0.0001**	0.0965	< **0.0001**	0.4750
S275	0.2646	< **0.0001**	**0.0001**	0.5015	0.8548	0.1082	0.3387
FI	< **0.0001**	< **0.0001**	**0.0001**	0.4487	0.8990	< **0.0001**	0.7457
HIX	< **0.0001**	< **0.0001**	< **0.0001**	< **0.0001**	< **0.0001**	0.0101	0.0532
BIX	< **0.0001**	< **0.0001**	0.0181	0.9695	**0.0006**	**0.0001**	0.5672
Ext. Nitrate	0.0075	< **0.0001**	**0.0004**	0.1034	0.0765	0.0049	0.9719
Ext. Ammonium	< **0.0001**	< **0.0001**	< **0.0001**	< **0.0001**	**0.0014**	0.2754	0.0909
Ext. SRP	< **0.0001**	0.2189	0.2662	0.2391	0.6319	0.8277	0.2801
PMN	< **0.0001**	0.0317	0.0575	0.1638	0.1470	0.9723	0.1068
PMP	< **0.0001**	< **0.0001**	0.0102	0.3945	**0.0015**	0.0268	0.5701
CH_4 Production	< **0.0001**	< **0.0001**	0.0057	< **0.0001**	0.0055	**0.0026**	0.0561
CO_2 Production	< **0.0001**	< **0.0001**	0.0054	< **0.0001**	0.0180	0.0276	0.4282
Fluorophore A	0.9489	0.0144	0.0638	0.9988	< **0.0001**	0.4052	0.9999
Fluorophore B	0.5879	**0.0020**	0.7735	0.9598	0.7081	0.6100	0.2944
Fluorophore T	0.9570	0.0059	0.0691	0.9988	< **0.0001**	0.3919	0.9999

to as "site"), distance inland, and depth, a linear model was used (fixed effects - direction, distance inland, depth; random effects - transect; package 'lme4'). A Bonferroni correction was applied to reduce the possibility of inflated Type I error due to the testing of multiple hypotheses (Bonferroni, 1936), lowering the alpha value to 0.003 (0.05/# of comparisons). PARAFAC via Matlab was used to model the dataset based on excitation and emission spectra created by the Spex Fluorolog-3. Component models were produced by applying parameters to the data set and minimizing the sum of squared errors by validation methods (core consistency, split half analysis) and removing them from the data. The component models were then interpreted for resulting fluorophore intensity to determine major sources and percent composition of DOM. Principle Components Analysis (PCA) was used to isolate correlations in the ecological and spectroscopic data at each of the sites, as well as statistically verify grouping of depths and variables. Correlation matrices were constructed using Pearson Product-Moment correlations to determine relationships between variables. The erosion rates on three different sides of the island were compared using a repeated measures ANOVA.

3. Results

3.1. Erosion rate

Analysis of satellite imagery since 1998 revealed site had a significant effect ($p < 0.001$) on erosion rate over time. The west side of the island consistently experienced the greatest erosion, with the marsh edge retreating approximately 85 m inland over a period of two decades. The greatest erosion rate (6.28 ± 0.34 m yr^{-1}) was observed between 1998 and 2005, with a 50 m inland retreat on the west side. The erosion rate decreased to 3.54 ± 0.56 m yr^{-1} between the year 2005 and 2012 (~25 m retreat), and 1.76 ± 0.58 m yr^{-1} between the year 2012 and 2018 (~10 m retreat). The erosion rates on other two sides (north and south sites) of the island were relatively constant over the last two decades (1998–2018) with approximate erosion rates of 0.77 m yr^{-1} on north side and 0.79 ± 0.04 m yr^{-1} on south side (retreating approximately 15 m and 16 m on north and south sides, respectively). Current field-measured erosion rates were 3.36 ± 0.4, 1.34 ± 0.2, and 0.58 ± 0.03 m yr^{-1} on the west, north, and south sides of island respectively.

3.2. Soil physicochemical characteristics

Moisture content differed with depth (Table 2), ranging from 74.95 ± 0.60% at 20–30 cm to 82.14 ± 0.82% at 70–80 cm. Moisture content was negatively correlated to bulk density, and strongly positively correlated to % OM, A_{254}, A_{350}, HIX, extractable NH_4^+, and extractable SRP (Table 3). Similarly, bulk density was predicted (Table 2) by depth, ranging from 0.194 ± 0.010 g cm^{-3} at 70–80 cm to 0.281 ± 0.016 g cm^{-3} at 40–50 cm (Table 4). Generally, bulk density increased from the surface to 40–50 cm, then decreased down to 100 cm. Bulk density was also predicted by the interaction between depth and site (Table 2), with lowest values at the west site at 70–80 cm (0.187 ± 0.007 g cm^{-3}) and greatest values at the west site at 40–50 cm (0.320 ± 0.038 g cm^{-3}). Bulk density was negatively correlated (Table 3) with % OM, A_{254}, A_{350}, HIX, and extractable NH_4^+ and SRP.

Depth was also a predictor of % OM, ranging from 27.04 ± 1.50% at 40–50 cm to 39.96 ± 1.47% at 70–80 cm (Tables 2 and 4). Organic matter decreased from the surface to 40–50 cm. At 50–60 cm, OM content increased roughly 30% and remained relatively constant through the rest of the depth profile (Table 4). The interaction of depth and distance inland also predicted OM content, ranging from an average of 24.7 ± 3.80% at 40–50 cm within the west site to an average of 42.1 ± 2.43% at 80–90 cm within the north site. Total C concentrations decreased from the surface to 30–40 cm

Table 3
Correlation matrix for each measured parameter (r values). Bold values indicate a positive correlation, while italicized values indicate a negative correlation. Only significant r values are shown. (n = 270, d.f. = 268, alpha = 0.001, critical value = 0.199).

	CO_2	CH_4	BD	MC	OM	TP	Sal	TN	TC	A_{254}	A_{350}	S_{275}	FI	BIX	HIX	Ext. NO_3^-	Ext. SRP	Ext. NH_4^+	PMN Rate
CH_4	–																		
BD	–	–																	
MC	–	–	*−0.97*																
OM	–	–	*−0.80*	**0.80**															
TP	–	–	–	–	–														
Sal	**0.31**	*−0.37*	–	–	–	–													
TN	–	–	*−0.37*	**0.36**	**0.31**	–	–												
TC	–	–	*−0.35*	**0.34**	**0.33**	–	–	**0.94**											
A_{254}	**0.33**	*−0.27*	*−0.24*	**0.28**	**0.25**	–	**0.33**	**0.40**	**0.29**										
A_{350}	**0.27**	*−0.26*	*−0.20*	**0.24**	**0.21**	–	**0.29**	**0.36**	**0.24**	**0.99**									
S_{275}	–	–	–	–	–	–	–	–	–	–	–								
FI	*−0.23*	**0.30**	–	–	–	–	*−0.32*	–	–	*−0.44*	*−0.41*	–							
BIX	–	**0.25**	–	–	–	–	*−0.26*	–	–	–	–	–	**0.77**						
HIX	–	*−0.44*	*−0.21*	**0.27**	**0.21**	–	**0.47**	–	–	**0.59**	**0.60**	–	*−0.59*	*−0.68*					
Ext. NO_3^-	–	–	–	–	–	–	*−0.22*	–	–	–	–	–	–	–	–				
Ext. SRP	–	–	*−0.37*	**0.38**	**0.39**	–	–	**0.26**	–	**0.54**	**0.51**	–	–	–	**0.27**	–			
Ext. NH_4^+	**0.25**	–	*−0.32*	**0.35**	**0.36**	–	–	**0.28**	–	**0.63**	**0.61**	–	*−0.25*	–	**0.34**	–	**0.65**		
PMN Rate	–	–	–	–	–	**0.35**	–		–	*−0.31*	*−0.31*	–	**0.24**	**0.27**	*−0.39*	–	–	*−0.22*	
PMP Rate	–	–	–	–	–	**0.44**	–	–	–	–	–	–	–	–	–	–	–	–	**0.49**

Table 4
Soil physicochemical properties by both site and depth. Values are means and standard errors, which are in parenthesis (n = 9).

Site	Depth (cm)	BD (g cm^{-3})	MC (%)	Total C (g kg^{-1})	Total N (g kg^{-1})	Total P (mg kg^{-1})	Organic Matter (g kg^{-1})
West	0–10	0.262 (0.013)	75.5 (1.02)	138 (12.5)	7.02 (0.748)	479 (31.2)	314 (28.7)
	10–20	0.281 (0.014)	74.6 (0.888)	123 (8.80)	6.28 (0.378)	454 (15.7)	296 (18.5)
	20–30	0.298 (0.012)	73.9 (1.11)	114 (15.0)	6.40 (0.561)	431 (16.2)	256 (16.3)
	30–40	0.275 (0.018)	75.6 (1.57)	111 (8.72)	6.18 (0.411)	430 (13.2)	269 (20.2)
	40–50	0.320 (0.039)	72.6 (2.97)	102 (18.9)	5.79 (1.03)	431 (12.6)	247 (37.9)
	50–60	0.213 (0.010)	81.3 (0.661)	175 (10.9)	9.25 (0.573)	436 (9.10)	387 (20.0)
	60–70	0.196 (0.011)	82.3 (0.900)	178 (10.4)	9.55 (0.424)	405 (21.4)	392 (22.6)
	70–80	0.187(0.007)	82.9 (0.647)	175 (9.71)	9.97 (0.532)	409 (18.9)	396 (19.0)
	80–90	0.213 (0.014)	80.3 (1.18)	156 (13.0)	9.38 (0.675)	386 (24.8)	363 (28.9)
	90–100	0.226 (0.020)	79.7 (1.70)	165 (26.2)	10.3 (1.62)	433 (14.2)	375 (52.1)
North	0–10	0.241 (0.015)	77.2 (1.19)	167 (15.3)	8.66 (0.772)	726 (73.2)	367 (32.5)
	10–20	0.249 (0.007)	77.1 (0.669)	154 (13.4)	7.84 (0.585)	480 (61.1)	309 (35.8)
	20–30	0.273 (0.014)	75.4 (1.19)	123 (11.6)	6.54 (0.468)	478 (23.3)	296 (20.44)
	30–40	0.235 (0.091)	78.5 (1.19)	110 (9.37)	6.03 (0.352)	444 (155)	272 (88.9)
	40–50	0.282 (0.021)	75.2 (1.63)	113 (6.89)	5.88 (0.371)	433 (12.7)	265 (11.3)
	50–60	0.230 (0.008)	79.1 (0.585)	140 (8.62)	7.20 (0.318)	438 (10.0)	392 (64.1)
	60–70	0.239 (0.027)	78.1 (2.26)	149 (20.2)	7.49 (0.964)	447 (14.3)	356 (43.3)
	70–80	0.187 (0.011)	82.3 (0.963)	187 (11.9)	9.62 (0.548)	438 (13.4)	407 (20.8)
	80–90	0.187 (0.011)	82.8 (0.891)	194 (12.8)	10.53 (0.519)	440 (7.50)	421 (24.2)
	90–100	0.217 (0.016)	79.9 (1.45)	168 (15.3)	9.51 (0.608)	413 (28.2)	380 (28.1)
South	0–10	0.230 (0.009)	76.6 (0.730)	151 (9.80)	7.83 (0.362)	688 (62.1)	345 (16.7)
	10–20	0.232 (0.007)	78.1 (0.624)	158 (10.2)	7.91 (0.326)	550 (39.3)	349 (14.8)
	20–30	0.271 (0.011)	75.6 (0.823)	120 (5.34)	6.56 (0.163)	412 (27.8)	291 (13.3)
	30–40	0.271 (0.005)	76.0 (0.349)	111 (3.82)	6.33 (0.191)	413 (11.1)	267 (7.93)
	40–50	0.242(0.016)	77.7 (1.42)	127 (11.1)	6.96 (0.532)	404 (26.8)	299 (21.2)
	50–60	0.227 (0.018)	79.4 (1.62)	156 (13.6)	8.43 (0.704)	420 (14.3)	349 (28.0)
	60–70	0.189 (0.008)	82.3 (0.738)	182 (6.67)	9.93 (0.413)	433 (27.5)	400 (23.1)
	70–80	0.207 (0.026)	81.2 (2.26)	178 (20.6)	9.82 (1.04)	445 (23.0)	396 (35.9)
	80–90	0.199 (0.015)	81.4 (1.18)	177 (11.3)	9.94 (0.559)	395 (27.8)	378 (27.2)
	90–100	0.188 (0.016)	81.7 (1.05)	179 (13.9)	10.7 (0.804)	426 (18.5)	397 (33.0)

(110.45 ± 7.41 g kg^{-1}), increased up to the depth of 70–80 cm (179.77 ± 14.37 g kg^{-1}), and then slightly decreased (Table 4). Total C was strongly positively correlated to moisture content, OM, TN, A_{254}, and A_{350} (Table 3). Similarly, TN decreased from the surface to 40–50 cm and then gradually increased (Table 2, Table 4). Total P was predicted by depth, distance inland, and the interactions between both depth and site (Table 2), but exhibited a different trend than other total soil nutrient pools, being highest at the surface (631 ± 38.7 mg kg^{-1}) and lowest at 80–90 cm (407 ± 13.0 mg kg^{-1}) (Table 4). Total P was positively correlated to potentially mineralizable N and P rates (Table 3).

Porewater salinity was affected by depth, site, distance, and the interaction between depth and site (Table 2), ranging from 19.5 ± 1.16 ppt at the surface (0–10 cm) to 26.8 ± 1.23 ppt at 40–50 cm. Salinity averaged 17.8 ± 0.43, 28.3 ± 0.34, and 26.6 ± 0.45 ppt at the west, north, and south sites, respectively. In terms of distance, salinity averaged 22.80 ± 0.617 ppt at 1 m inland, 24.68 ± 0.578 ppt at 3 m inland, 25.21 ± 0.683 ppt at 5 m inland. Salinity was positively correlated to A_{254}, A_{350}, CO_2 production, and HIX, and negatively correlated to CH_4 production, FI, BIX, and extractable NO_3^- content (Table 3).

3.3. Spectroscopic indicator analyses

The UV–Vis indicators A_{254} and A_{350} increased with depth, indicating higher aromatic C storage with depth (Table 2, Fig. 3). A_{254} also differed with distance inland, the interaction between site and depth, and the interaction between site and distance inland (Fig. 3, Table 2). A_{254} ranged from a maximum intensity of 0.57 ± 0.04 within the west site at 90–100 cm to a minimum intensity of 0.24 ± 0.03 within the north site at 0–10 cm (Fig. 3). When considering the interaction between distance inland and site, A_{254} intensity ranged from an average 0.30 ± 0.02 at the west site 1 m inland to an average of 0.47 ± 0.02 at the north site 5 m inland (Fig. 3). Similarly, A_{350} differed with depth, site, distance inland, and the interactions between both depth and site and site and distance inland (Table 2, Fig. 3). Intensity ranged from an average of 0.05 ± 0.01 within the north site at 0–10 cm to an average of 0.14 ± 0.01 at the west site at 90–100 cm (Fig. 3). In terms of the interaction between site and distance inland, A_{350} values ranged from an average intensity of 0.07 ± 0.01 at the north 1 m inland location to 0.11 ± 0.01 at the north 5 m inland location (Fig. 3). The S_{275} intensity differed with both site (0.33 ± 0.01 south to 0.39 ± 0.01 north) and distance (0.33 ± 0.01 at 5 m to 0.37 ± 0.01 at 1 m), but not depth (Fig. 3). Both A_{254} and A_{350} were positively correlated to each other, CO_2 production, HIX, and extractable SRP and NH_4^+, while negatively correlated to CH_4 production, FI, and PMN (Table 3). S_{275} showed no significant correlations (Table 3).

The FI, an indicator of C source, was significantly different depending on the depth, site, and distance inland, as well as the interaction between site and distance inland (Table 2, Fig. 4). Fluorescence index values ranged from 0.96 ± 0.01 at the west site 1 m inland, to 0.87 ± 0.01 at the north site 3 m inland (Fig. 4). All recorded FI intensities were indicative of terrestrial-sourced C. Overall, the north site has the lowest FI intensity of all the sites (Fig. 4). Fluorescence index was positively correlated with CH_4 production, BIX, and PMN, while negatively correlated to CO_2 production, HIX, and extractable NH_4^+ (Table 3). The BIX differed in depth*distance and site* distance interactions, as well as by site and depth (Table 2, Fig. 4). Intensities ranged from 0.51 ± 0.02 at 30–40 cm 3 m inland to 0.67 ± 0.05 at 0–10 cm 1 m inland (Fig. 4). BIX was positively correlated to CH_4 production and extractable NH_4^+ and negatively correlated to HIX (Table 3). In general, HIX intensities increased with depth (Fig. 4, Table 2). Both the interactions between site*depth and depth*distance were also significant with HIX intensities, which ranged from 0.72 ± 0.03 at the west site at 0–10 cm, to 0.93 ± 0.01 at the north at 90–100 cm sample (Fig. 4). HIX was positively correlated to extractable SRP and NH_4^+, while negatively correlated to PMN and CH_4 production (Table 3).

A 3-component model was constructed through PARAFAC analyses. From highest to lowest fluorescence intensity, the fluorophores were

Table 5
PARAFACs fluorophore variables derived from UV–Vis analysis and fluorescence EEM data (modified from Haywood et al., 2019).

Measurement	Description	Chemical information	Ecological information	References
Fluorophore A	Combination of UV humic-like and aquatic-like (autochthonous sourced) material	Lower degree of conjugation and abundance of functional groups; aromatic, carboxyl, and hydroxyl	Aquatic-like sourced, recently produced material	Cook et al. (2009); Berlman (2012); Coble (1996); Parlanti et al. (2000)
Fluorophore T	Combination of visible humic-like and soil fluvic acid (allochthonous sourced) material	Increase conjugation and abundance of functional groups; aromatic, carboxyl, and hydroxyl	Terrestrial-like sourced, older material	Cook et al. (2009); Berlman (2012); Coble (1996); Parlanti et al. (2000)
Fluorophore B	Biological sourced DOM	Protein-like DOM in system	Result of biological activity	Coble (1996); Ghisaidoobe and Chung (2014)

identified as: Fluorophore T (Ex/Em: 265 (3 7 5)/540 nm), Fluorophore A (Ex/Em: 270/415), and Fluorophore B (Ex/Em: 275/335). Fluorophore B intensity was the only variable showing significant differences by site (Table 2). Each fluorophore indicates the source material of the porewater DOM (Table 1).

3.4. Greenhouse gas production

Both depth and site, as well at the interaction between the two, predicted CO_2 and CH_4 production (Table 1). Methane production was highest at the west site, averaging 2.52 ± 0.65 μg CH_4-C g^{-1} d^{-1}, and lowest at the north site, averaging 0.05 ± 0.01 μg CH_4-C g^{-1} d^{-1} (Fig. 5). The south site had an intermediate rate of methane production, with an average of 1.34 ± 0.32 μg CH_4-C g^{-1} d^{-1}. Methane production was greatest within the top two depth intervals, then precipitously decreased with depth (Fig. 5). Methane production was also predicted by the interaction between site and distance (Table 1). In terms of site, CO_2 production rates were the inverse of CH_4 production rates; CO_2 production was lowest in the west site (1.00 ± 0.08 μg CO_2-C g^{-1} h^{-1}), greatest at the north site (3.58 ± 0.32 μg CO_2-C g^{-1} h^{-1}), and intermediate at the south site (1.32 ± 0.08 μg CO_2-C g^{-1} h^{-1}) (Fig. 5). At the west and south sites (which had the highest and lowest erosion rates, respectively), CO_2 production was highest at the surface, decreased down to 30 cm, and then remained relatively constant from 30 to 100 cm (Fig. 5). However, the north site exhibited a different trend, where higher concentrations were observed between 40 cm and 100 cm and lower concentrations in the top 40 cm. Carbon dioxide production was significantly correlated with A_{254}, A_{350}, and extractable NH_4^+, while negatively correlated to FI (Table 2). Methane production was positively correlated with FI and BIX, but negatively correlated to A_{254}, A_{350}, and HIX (Table 2).

3.5. Extractable nutrients and potential mineralization rates

Both site and distance inland affected extractable NO_3^- concentrations (Table 2). Extractable NO_3^- was greatest within the west site, with an average concentration of 3.52 ± 0.287 mg kg^{-1}, compared to 0.847 ± 0.131 mg kg^{-1} and 2.14 ± 0.255 mg kg^{-1} at the north and south sites, respectively. In terms of distance inland, extractable NO_3^- concentrations ranged from 2.14 ± 0.67 mg kg^{-1} at 1 m inland to 2.62 ± 0.357 mg kg^{-1} at 5 m inland. Extractable SRP concentrations were only affected by depth (Table 2, Fig. 6). Concentrations generally increased with depth; the greatest extractable SRP concentrations were found at the lowest depth (90–100 cm), averaging 4.98 ± 0.656 mg kg^{-1} (Fig. 6). Concentrations were lowest at the 10–20 cm depth, averaging 0.724 ± 0.148 mg kg^{-1} (Fig. 6). Extractable SRP was positively correlated to extractable NH_4^+, A_{254}, A_{350}, and HIX, while negatively correlated to bulk density (Table 2). Extractable NH_4^+ differed by depth, site, distance inland, and the interactions of depth*direction and depth*distance (Table 1). Extractable NH_4^+ concentrations increased with depth, ranging from below detection at the surface to 71.6 ± 9.20 mg kg^{-1} at 90–100 cm (Fig. 6). Extractable NH_4^+ concentrations at the west, north, and south sites averaged 23.4 ± 5.14 mg kg^{-1}, 25.5 ± 2.76 mg kg^{-1}, and 20.8 ± 2.86 mg kg^{-1}, respectively (Fig. 6). Concentrations of extractable NH_4^+ were positively correlated with A_{254}, A_{350}, and HIX, but negatively correlated to FI (Table 2).

Potentially mineralizable N rates were only predicted by depth, while PMP rates were both predicted by depth and site, as well as the interaction between depth and distance inland (Table 1). Potentially mineralizable N rates were generally greatest at the surface, averaging 39.3 ± 3.38 mg kg^{-1} d^{-1}, and lowest at the 90–100 cm depth interval, averaging 14.5 ± 1.00 mg kg^{-1} d^{-1} (Fig. 5). PMP was lowest at the west site, where rates averaged 0.51 ± 0.092 mg kg^{-1} d^{-1}, and highest at the north site, averaging 1.27 ± 0.254 mg kg^{-1} d^{-1}

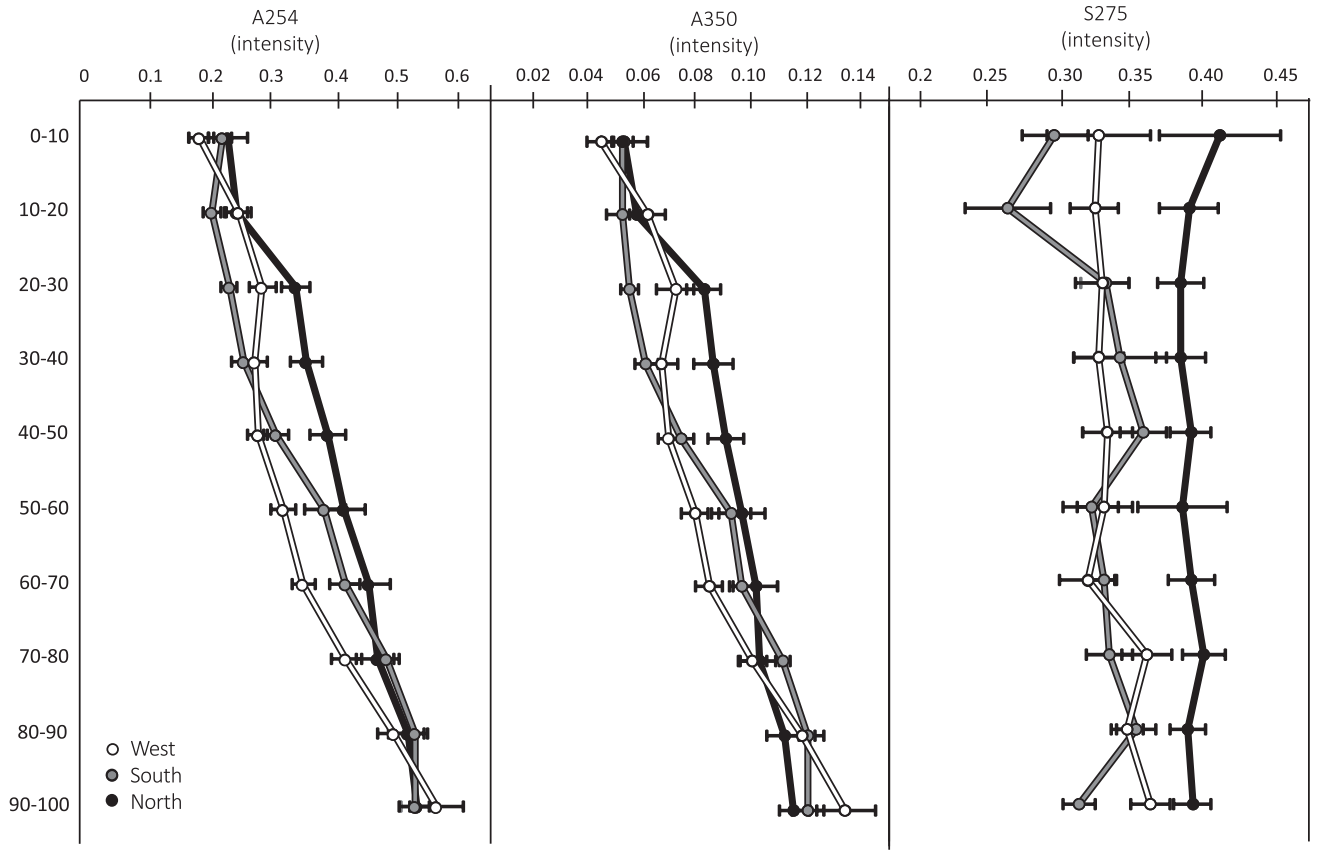

Fig. 3. UV–Vis indicators (A_{254}, A_{350}, and S_{275}) plotted with depth at each site. Each point represents mean of distances inland and replicates ± standard error (n = 9).

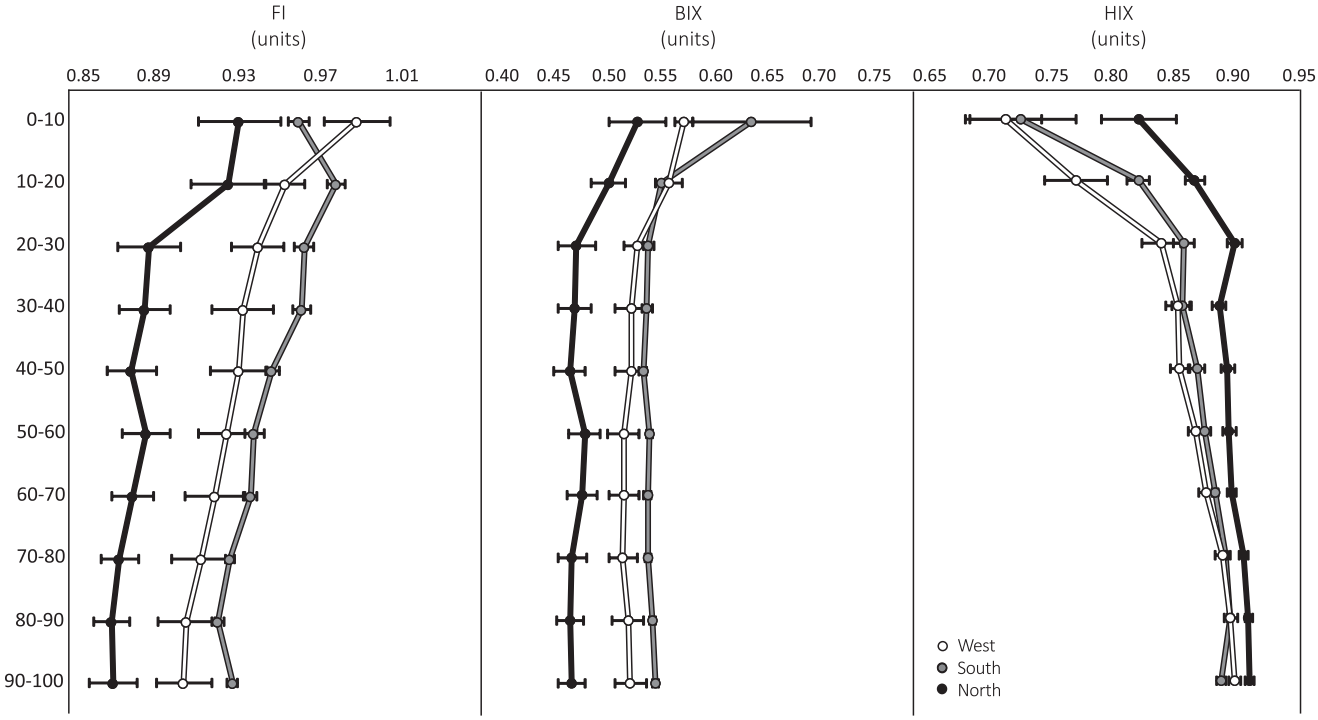

Fig. 4. Fluorescence indicators (FI, BIX, HIX) plotted with depth at each site. Each point represents mean of distances inland and replicates ± standard error (n = 9).

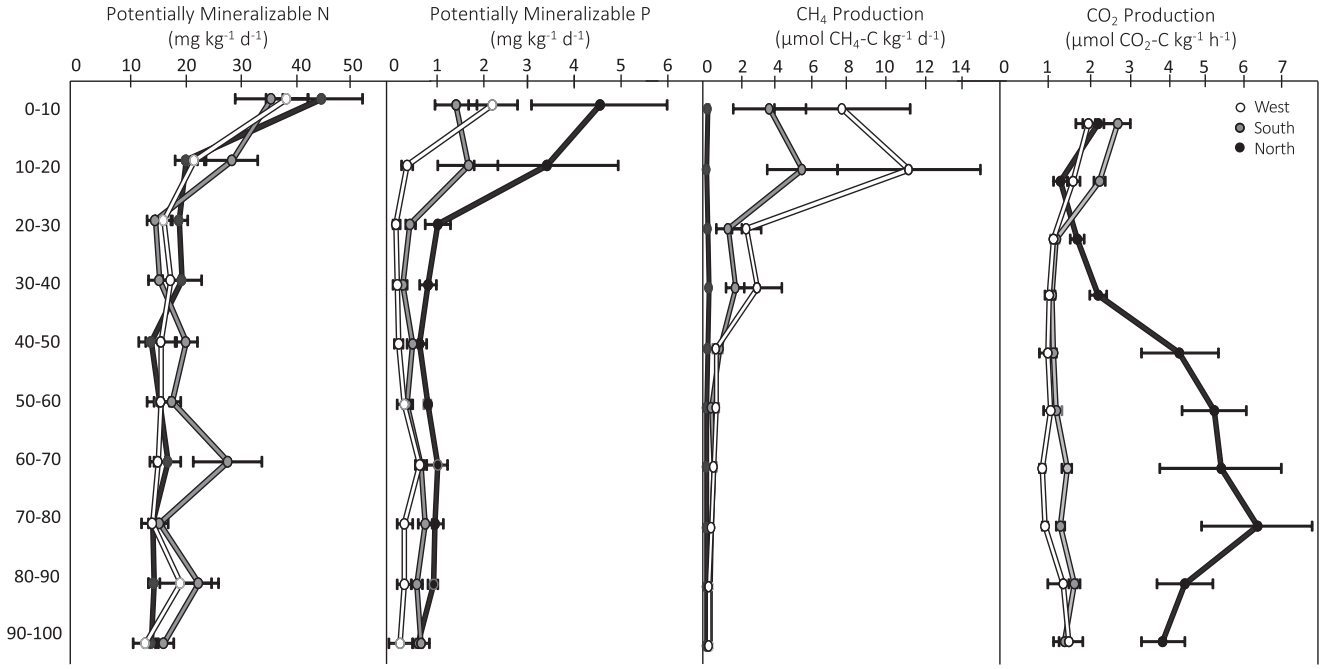

Fig. 5. Depth profile of potentially mineralizable N, potentially mineralizable P, rate of CH_4 production, and rate of CO_2 production from each site. Each point represents mean of distances inland and replicates ± standard error (n = 9).

(Fig. 5). In terms of the interaction between depth and distance inland, PMP rates ranged from 0.249 ± 0.099 mg kg^{-1} d^{-1} at 1 m inland 40–50 cm to 4.40 ± 1.52 mg kg^{-1} d^{-1} at 5 m inland 10–20 cm (Fig. 5). Generally, PMP rates were highest at the surface, where they averaged 2.79 ± 0.597 mg kg^{-1} d^{-1} (Fig. 5). PMP rates decreased precipitously between 10 and 20 cm and 20–30 cm; below 30 cm, PMP rates were relatively constant (Fig. 5). Potentially mineralizable N rates were correlated with PMP rates (Table 2).

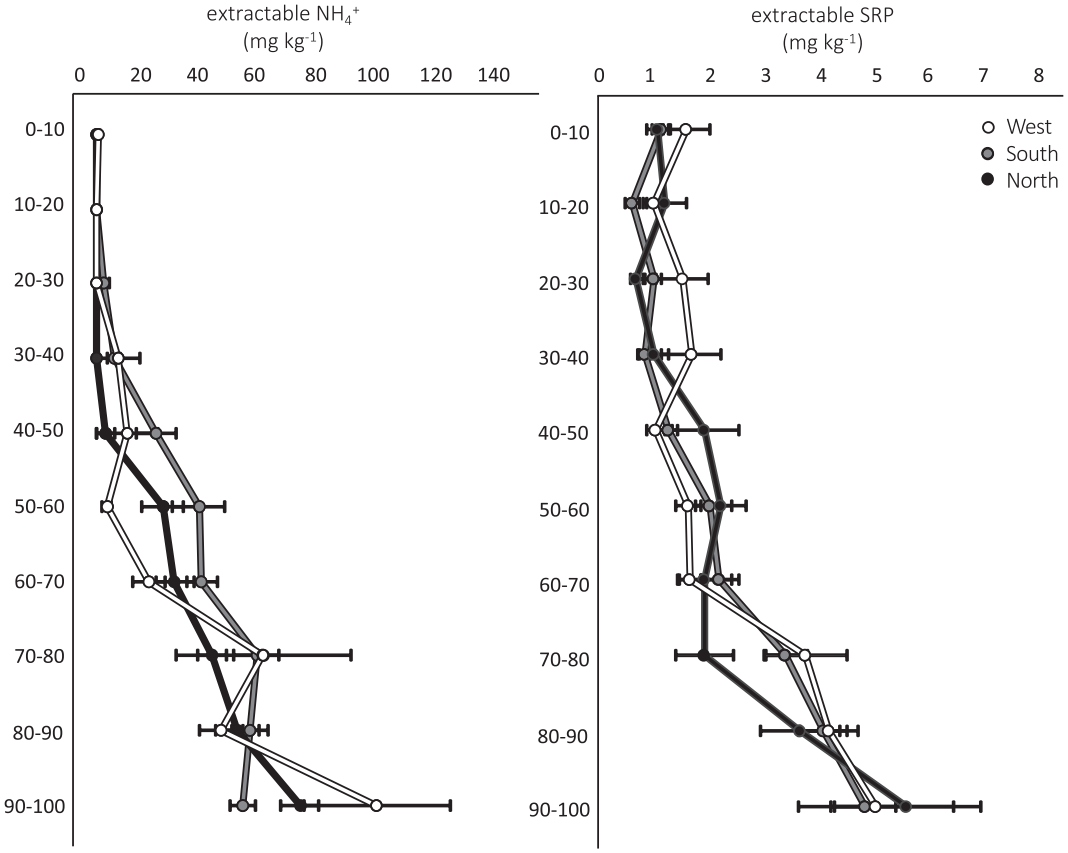

Fig. 6. Depth profile of Extractable NH_4^+ and Extractable SRP from each site. Each point represents mean of distances inland and replicates ± standard error (n = 9).

4. Discussion

4.1. Site erosion and wetland loss

Barataria Bay has some of the highest rates of relative sea level rise in the world (12 mm yr^{-1}) (Jankowski et al., 2017), which has contributed to a wetland loss rate of 13.33 km^2 yr^{-1} (Couvillion et al., 2017). Therefore, coastal Louisiana is experiencing rates of sea level rise (and associated wetland loss) today that the rest of the world is predicted to experience in the next 50–80 years (Horton et al., 2014). As the area of wetlands lost to submergence increases, the fetch length next to the remaining marsh islands also increases, enhancing the intensity of wind-driven waves which, in turn, increases erosion rates, promote fragmentation, and consequently increase shoreline lengths that are susceptible to further erosion. Although marsh edge erosion is a continuous process (Leonardi et al., 2016a) in Barataria Basin, the rates of erosion vary over space and time. Observations from our study site suggest that the most severe erosion occurs at low tide, when wave energy scours the less consolidated soil near the lower portion or the root zone, creating an escarpment with a flap of densely interwoven roots and vegetation at the surface that is temporarily more resistant to wave erosion (Tonelli et al., 2010; Valentine and Mariotti, 2019). Conversely, at high tide the marsh platform is submerged, causing the wave energy to propagate and dissipate over a much larger area. The continuous process of erosion at marsh edge exposes new soil surfaces to the action of wave energy, progressively converting additional marsh area into open water. The rapid and continuous nature of the erosion at this site has led to equally rapid shifts in vegetation zonation, as seen by the presence of terrestrial shrubs ~6 m inland from the edge of the marsh on all directions.

In the previous two decades, the island has demonstrated continuous erosion, however, the rate remains dynamic. The west side of the island was most dynamic in terms of erosion rate, generally decreasing over time. The west side of the island has a longer fetch and the bay is deeper in comparison to north and south sides (Sapkota and White, 2019a,b) resulting in the higher erosion rate. The greatest erosion rates observed from 1998 to 2012 is mainly due to the fragmentation and submergence of surrounding pieces of the marshes, as evidenced by the time series of Google Earth. The moderate erosion on the north side of the island may be due to refraction of waves from the west side and the waves created by relatively strong northerly wind during the winter. The south side of the island is relatively sheltered, with lower wave energy, which results in slower erosion rates.

Differences within the measured soil characteristics, both by site and by soil depth, were not directly attributed to erosional magnitude. However, these spatial differences observed between sites on the island could be an indirect product of past erosion rates. As erosion progresses, the soils along the edge of the wetland are lost to the surrounding bay, and soils that were previously more inland are exposed. In 1998, the west site was previously 85 m inland, and, as vegetation zonation in wetlands is mediated by distance inland and micro-topographical changes, likely supported a different vegetation community than at the time of sampling. Historical aerial imagery shows that as the island erodes, the extent of *Iva frutescens* decreases while *Spartina alterniflora* extent increases, occupying the edges of the island. Vegetation communities are responsible for the majority of C inputs within brackish wetlands within Barataria Bay (Feijtel et al., 1985), and thus differences between the past vegetation communities at each site could be responsible for the observed differences in C properties both between sites and with depth. Resident vegetation can also mediate stores of inorganic N and P, and indirectly affect the breakdown of OM through associated microbiota (Reddy and DeLaune, 2008).

4.2. Physical and chemical characterization of marsh soils and porewater

Depth was a significant predictor of 18 out of 20 biogeochemical and spectroscopic indicators measured. Generally, both biogeochemical and spectroscopic indicators were distinctly different between the upper 30 cm of the soil and porewater profile and the lower 70 cm, as demonstrated by the PCA (Fig. 7); the data was subsequently separated into two depth 'bins': 0–30 cm and 30–100 cm. The upper 30 cm of the soil profile contains the active root zone where biological processes dominate, as indicated by relatively higher BIX values within the porewater, as well as greater soil PMN, PMP, CH_4, and CO_2 production (south and west sites, Fig. 5). Spectroscopic measurements of aromaticity, A_{254} and A_{350}, indicate an increasing amount of porewater aromatic DOM with depth (Fig. 3), which is likely a result of decomposition of this material acting on labile components of the porewater

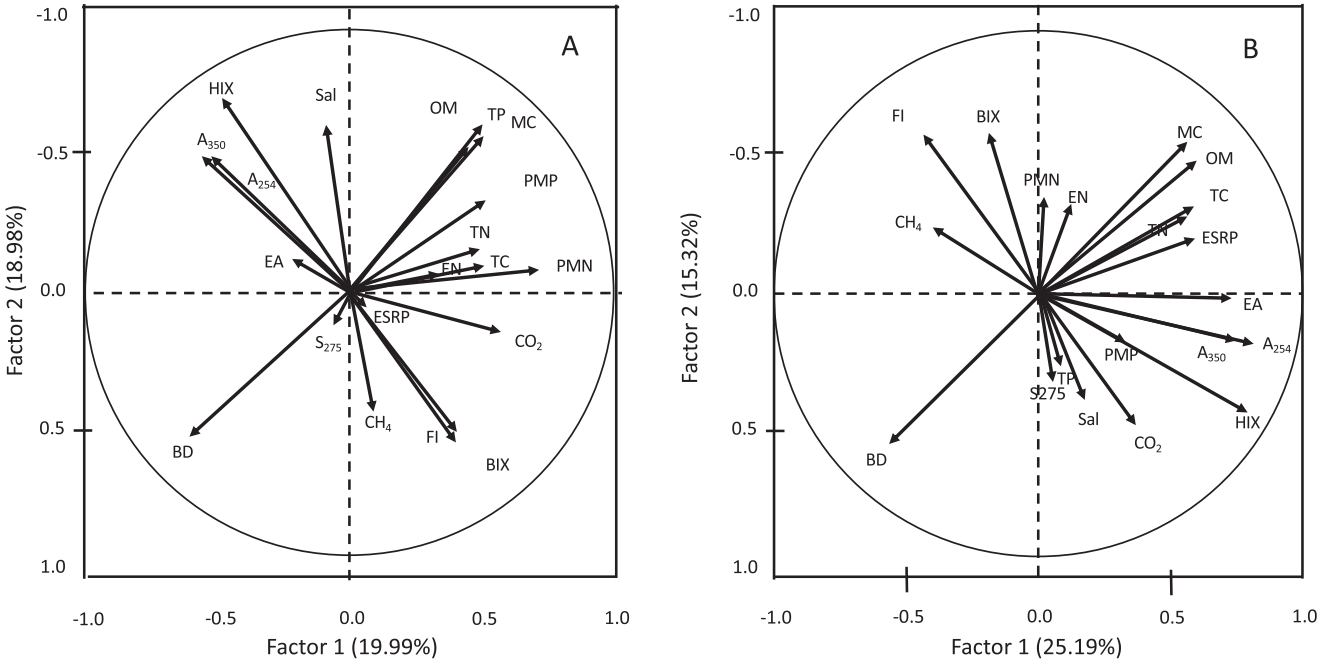

Fig. 7. Principle component analysis of each measured parameter at the top depths (A; 0–30 cm) and bottom depths (B; 30–100 cm).

and preserving the more recalcitrant/aromatic component. When combined, these spectroscopic analyses (BIX, HIX, A_{250}, A_{350}) demonstrate that the surficial porewater DOM can be characterized as autochthonous, non-humified, lower molecular weight C compounds with a lower amount of aromatic moieties than observed within the porewater at greater depths (Fig. 3, Table 1). Thus, this relatively labile porewater DOM can be readily utilized as an electron donor by resident microbiota to facilitate microbial respiration. As microbial abundance is greatest within the surficial soils (i.e. the active root zone; Steinmuller and Chambers, 2019), the combination of abundant, active microbes and labile organic C sources likely drives the increase in microbial measures such as PMN, PMP, and greenhouse gas production observed at the surface. Seemingly counterintuitively, DOM quality (spectroscopic measurements) is not significantly correlated to the measures of biological activity (Table 3), likely due to either a) the different matrices of each analysis (i.e., porewater versus porewater + soil, Table 1), or b) high availability of C coupled with low microbial demand.

Deeper than 30 cm, biological processes no longer dominate biogeochemical transformations, particularly within porewater DOM (Haywood et al., 2019) and both microbial measures (mineralization of N and P, CO_2 production) and BIX intensity remain relatively constant as depth increases. A_{254}, A_{350}, and HIX steadily decrease with increasing depth, indicating that porewater DOM gradually increases in molecular weight, amount of aromatic moieties, and degree of humification, similar to the conclusions of Haywood et al. (2019) from another location within Barataria Bay, LA. These trends are likely indications of different soil source material, such as historic plant communities, present at different depths (DeLaune, 1986). In contrast, these trends could hold with the theory of selective preservation (Lützow et al., 2006; Sollins et al., 1996), where labile components of organic material decrease with increasing degree of decomposition (i.e. depth). However, this theory of soil organic matter stabilization has not, to our knowledge, been previously applied to porewater DOM, and has recently been brought into question regarding its importance within coastal wetland systems (Steinmuller and Chambers, 2019).

Within the north site, CO_2 production at the greatest depths was approximately 3 times that of the top 30 cm (Fig. 5), which seems to contradict the increases in molecular complexity of DOM suggested by the spectroscopic measurements, as well as general assumptions concerning decreases in microbial activity with increasing depth. However, this trend is comparable to CO_2 production observed within cores taken in a now-eroded area of this site (Steinmuller et al., 2019), where CO_2 production increased precipitously from 50 to 100 cm and was attributed to changes in OM content. Our data indicates that % OM is consistent at all sites, suggesting the differences in CO_2 production between the north site and the other two sites could be driven by either functional differences within the microbial community or changes in labile constituents within the soil matrix itself, rather than the porewater.

4.3. Comparisons of analytical approaches

A thorough understanding of the physical and chemical properties that comprise the soils of coastal wetlands threatened by erosion is critical to our ability to (i) predict their fate following submergence (i.e., mineralization vs. burial), (ii) produce accurate biogeochemical models of coastal C and nutrient dynamics under future climate change scenarios, and (iii) understand the physical and chemical effects of erosion. Over the last several decades, key biogeochemical properties have emerged within the scientific literature as standardized, repeatable metrics for assessing the availability of long-turnover/stable soil nutrient pools (e.g., % OM, TC, TN, TP), short-turnover/bioavailable nutrient pools (e.g., porewater and extractable NH_4^+, NO_3^-, SRP), and soil mineralization rates (e.g., CO_2 and CH_4 production, PMN, and PMP) (Bridgham and Ye, 2013; Reddy and DeLaune, 2008). More recently, aquatic geochemists have begun developing and employing spectroscopic measurements and indices for surface and porewater in attempt to better discriminate between the sources and structure of porewater DOM, as well as determining the degree of biological processing or humification (Coble, 1996). To our knowledge, this paper represents the first study to couple analyses of soil biogeochemical properties with spectroscopic porewater DOM analyses on the same samples in order gain a comprehensive perspective of coastal wetland soil properties. In doing so, we also have an opportunity to evaluate how these two approaches compare with one another (Table 1).

Generally, there were few significant correlations between spectroscopic measurements and biogeochemical measurements, which can be attributed to the different analysis matrices. Although porewater DOM properties are considered to be a direct reflection of soil chemistry (Coble, 1996) the specific analytical substrates differ from those used for soil biogeochemical analysis. Spectroscopic measurements use soil porewater (centrifuged and decanted), while traditional biogeochemical measurement use either the soil solids in isolation (e.g., % OM, TC, TN, TP), the entire soil matrix (solids and porewater; e.g., greenhouse gas production and nutrient mineralization rates) or the combination of porewater and soil nutrients adsorbed to the soil exchange complex (extractable NH_4^+, NO_3^-, SRP). In correlating the soil biogeochemical analyses to the spectroscopic analyses, we elected to only address correlations with r values $>$ 0.6 (indicative of a moderate to strong correlation), despite the critical r value (correlation coefficient) being 0.199 due to the large sample size (270 soil samples). As a result, only a few correlations between spectroscopic measurements of porewater DOM and soil biogeochemical properties demonstrated a strong relationship: the correlations between A_{254}, A_{350}, and extractable ammonium (see Section 4.3).

Utilizing the principle components analysis (Fig. 7), it is evident that certain parameters explain the distribution of data better than other parameters. Specifically, soil physicochemical measurements (TC, TN, OM, MC, and BD) as well as HIX, A_{254}, and A_{350} are farther away from the origin and closer to the correlation circle. These soil physicochemical properties both act as long-term pools of soil nutrients and critical regulators of biogeochemical cycling within wetland soils, and the importance of HIX, A_{254}, and A_{350} within the PCA demonstrates comparability between these spectroscopic measurements and soil physicochemical parameters. Total soil nutrients support biogeochemical cycling within soils, and act as long-term indicators of soil nutrient cycling (Reddy and DeLaune, 2008, Table 1). Based on the comparability among these soil physicochemical properties, we hypothesize that porewater DOM represents an integrated, long-term indicator of porewater DOM quality, quantity, and source material.

4.4. Interactions between erosion, bay water incursion, and soil properties

The impact of erosion magnitude on soil properties is most identifiable by changes in C quality and microbial activity. While higher values of A_{254} and A_{350} at the north site indicate a higher amount of aromatic DOM than within the south and west sites, the greater S_{275} values suggest this DOM consists of lower molecular weight C. The labile nature of this C, despite containing aromatic compounds, can be attributed to the greater CO_2 production observed within the north site. The labile C present within porewater DOM at the north site is likely only a partial contributor to dramatic increase in CO_2 production with depth.

The west and south sites displayed high BIX values, indicating that the porewater DOM at these sites is more autochthonous, rather than allochthonous DOM, produced by microbial byproducts or vegetative input (Table 1). Additionally, the upper layer of soil (0–40 cm) in the west and south sites produced more methane than the north site, likely a result of the observed greater salinity at the north site, which may drive the microbial community towards sulfate reduction rather than methanogenesis (Delaune et al., 2002). Consequently, the south and west sites exhibit lower conductivity and CO_2 production while sustaining higher rates of methanogenesis within the top 40 cm.

There was little evidence of bay water incursion into the soil platform. Instead, salinity was shown to increase with distance inland, indicative of less frequent flushing and possibly the accumulation of salts due during evaporation. Therefore, changes in soil properties by distance are likely the result of differences in stable, long-term nutrient pools, possibly associated with vegetation transitions, as opposed to bay water incursion (Table 3). A general trend of increasing aromatic carbon and humification with distance inland, as indicated by porewater DOM A_{254}, A_{350}, and HIX values, imply a build-up of C in the inner part of the island (Figs. 3 and 4). In the west site, FI intensity between the 1 m and the 5 m distance decreases while values within the north and south sites stay consistent throughout the transect. While all FI measurements indicate terrestrially-derived porewater DOM, the fluctuation within FI values at the west site illustrates a relative increase in terrestrial inputs (rather than microbial inputs) with distance inland.

Though there is some evidence of interactions between soil properties and erosion rates, the influence of erosion was surprisingly minimal. While several soil parameters differed by site, these differences showed no clear trend in relation to erosion rates (Table 2). Soil properties in these sites, based on PCA, may be more controlled by soil physicochemical characteristics and measures of source and quality of C (HIX, A_{254}, and A_{350}). These parameters likely overshadow the impact of erosion, regardless of magnitude, until the marsh soil is actually eroded in to the bay.

4.5. Research limitations

Though the experimental design of this study allows for determining the impacts of erosional magnitude and saltwater incursion within this marsh platform, it must be acknowledged that the results of this study are site-specific. The dynamic nature of the wetlands within Barataria Bay is unique, specifically in its depositional history (Steinmuller and Chambers, 2019), and thus these results may not be applicable to other systems. Similarly, the comparisons between soil and porewater chemistry are imperfect due to the different matrices within each analysis. As these comparisons are novel, further scrutiny is required to develop a schematic for a more refined leveraging of these results.

4.6. Ecosystem implications

A significant result of this study was the observation of high concentrations of both extractable NH_4^+ and SRP present at deep depths (Fig. 6). Extractable nutrient concentrations are pools of bioavailable nutrients regulated by biological demand for inorganic nutrients, which catalyzes the mineralization of organic matter (Roy and White, 2013). As a result of biological uptake, likely by vegetation, the concentrations of both extractable NH_4^+ and SRP are low within the root zone (0–30 cm) across all sites (Fig. 6). However, below the root zone, both NH_4^+ and SRP concentrations increase dramatically; at 90–100 cm, concentrations of SRP and NH_4^+ are roughly 5x and 680x the concentrations at the surface, respectively (Fig. 6). The minimal biological activity supported by these deep soils does not facilitate uptake of these nutrients and thus these concentrations have likely increased over time due to microbial activity while remaining immobilized below 30 cm.

The continual erosion of this marsh platform has the potential to liberate these nutrients and release them into the surrounding bay. Extrapolation of current erosion rates measured within this study indicate that the entirety of the marsh platform from this study could be eroded by 2025. Assuming no changes in biological uptake and a loss of the entire 1 m depth interval, the conversion of this 1000 m^2 island to open water could result in roughly 520,000 mg of NH_4^+ and 47,000 mg of SRP (calculated to a depth of 1 m) fluxing into Barataria Bay and the Northern Gulf of Mexico (NGOM) from this island alone. While the whole meter of the soil matrix within the marsh platform might not be lost, both wave energy and erosion can contribute to the scouring of these low bulk density soils and flushing of porewater, which can exacerbate nutrient release. Extrapolating concentrations of labile nutrients and erosion rates to the entirety of Barataria Bay, which has an estimated area of 2,712 km^2 (Couvillion et al. 2017), we can estimate that 13.3 kg of NH_4^+ and 1.2 kg of SRP will be exported into the surrounding coastal zone over this timescale. Coastal outwelling of nutrients has been shown to affect the hypoxia zone that forms annually off the coast of Louisiana (Bianchi et al., 2010, 2008; Dagg et al., 2007). In particular, high concentrations of biologically-available N and P from the Mississippi River outflow catalyze phytoplankton blooms within the surface waters of the NGOM (Rabalais et al., 2002). Though modeling of C and N exports from Barataria Bay have demonstrated that fluxes from Barataria Bay to the NGOM are relatively small compared to nutrients supplied by the Mississippi River, studies have not considered the magnitude of labile stores of nutrients at depth within coastal wetlands. While it is important to note that not all the bioavailable nutrients lost during erosion will be transported to the coastal ocean, these estimates still include a large volume of N and P that can have deleterious impacts on the surrounding environment.

In addition to outwelling of labile N and P, the complete loss of this island through erosion represents a significant store of C that can be lost to various processes: bacterial mineralization in the aerobic water column, resuspension and deposition onto other marsh platforms, burial within bay sediments, or export as particulate OM into the coastal ocean. Similar calculations, as referenced above, yield that over the same timescale, 214,667 kg OM could be lost. In an experimental study, Steinmuller et al. (2019) observed a 66% increase in mineralization of C between anaerobic and aerobic soils from within Barataria Bay, demonstrating that significant portions of C could be lost through bacterial mineralization within the oxygenated water column. Similarly, through organic C fractionation from soils at a similar site, Steinmuller and Chambers (2019) determined that soil organic matter ranged from 17 to 30% labile constituents. The labile nature of this soil C indicates that mineralization can proceed rapidly, resulting in a net loss of C either as dissolved organic C in the water column or CO_2 in the atmosphere. In addition to microbial respiration, bulk density values within the bay indicate that organic matter exported from wetlands through erosion is not being reburied (Vaccare et al., 2019). It can be inferred that portions of C lost through wetland erosion are either redeposited on other marsh platforms, lost as CO_2 to the atmosphere (Sapkota and White, 2019b), and exported to the surrounding coastal ocean as DOC.

5. Conclusions

The interactive effect of both physical and chemical processes on marsh soil properties has not been well-documented, despite this knowledge being invaluable to understanding erosive collapse in brackish and saltwater coastal marshes. In an eroding coastal marsh in Barataria Bay, Louisiana, depth was the dominant driver of the majority of measured spectroscopic and biogeochemical parameters (18/20). Biological processes dominated soil and porewater transformations in the upper (0–30 cm) layers of soil, likely due to the presence of low molecular weight labile C substrates that support microbial communities and activity. However, at greater soil depths (30 cm+), where higher molecular weight C substrates and humified compounds persisted, physicochemical transformations dominated soil and porewater properties. We did not find evidence of salt water incursion into the soil profile, even at 1 m distance from the marsh edge, nor were there strong correlations between erosion rates and marsh soil properties. However, we did find that regardless of erosion rates, soil characteristics were largely controlled by physicochemical characteristics (TC, TN, OM, moisture content, & bulk density) and spectroscopic measurements of porewater DOM quality (HIX, A_{254}, and A_{350}).

This study suggests that prior to soil erosion and subsequent removal from the marsh platform, erosion only has a minimal impact on

marsh soil properties, though future research should focus on determining whether this is a site-specific result. The large pools of extractable NH_4^+ and SRP found at depth within this site, represent pools with the potential to be liberated with continued erosion into Barataria Bay, and possibly transported to the coastal ocean where it could contribute to hypoxia in the NGOM. In order to characterize this export, future controlled experimental manipulations are required to determine the extent, fate, and potential impacts of this release of labile nutrients.

This study is the first to couple biogeochemical and spectroscopic analyses to evaluate soil marsh properties, providing a comprehensive understanding of soil characteristics in an eroding coastal marsh. As a novel combination of analyses, continued work is required to refine how to leverage the combination of these results and their inherent different matrices to synthesize a valuable and more holistic insight to soil and porewater structure in coastal wetlands.

Declarations of Competing Interest

The authors declare that they have no known competing financial interests or personal relationships that could have appeared to influence the work reported in this paper.

Acknowledgements

The authors wish to acknowledge Peter Mates, Chelsea Nitsch, and Hayden Denton for assistance with field sampling and laboratory analysis. This work was supported through a collaborative National Science Foundation Chemical Oceanography Grant (#1635837).

Appendix A. Supplementary material

Supplementary data to this article can be found online at https://doi.org/10.1016/j.catena.2019.104373.

References

Ardón, M., Helton, A.M., Bernhardt, E.S., 2016. Drought and saltwater incursion synergistically reduce dissolved organic carbon export from coastal freshwater wetlands. Biogeochemistry 127, 411–426. https://doi.org/10.1007/s10533-016-0189-5.

Bianchi, T.S., Dimarco, S.F., Allison, M.A., Chapman, P., Cowan Jr, J.H., Hetland, R.D., Morse, J.W., Rowe, G., 2008. Controlling hypoxia on the US Louisiana shelf: beyond the nutrient-centric view. Eos. Trans. Am. Geophys. Union 89, 236–237.

Bianchi, T.S., DiMarco, S.F., Cowan Jr, J.H., Hetland, R.D., Chapman, P., Day, J.W., Allison, M.A., 2010. The science of hypoxia in the Northern Gulf of Mexico: a review. Sci. Total Environ. 408, 1471–1484.

Bonferroni, C.E., 1936. Teoria statistica delle classi e calcolo delle probabilità, Pubblicazioni del R Istituto Superiore di Scienze Economiche e Commerciali di Firenze.

Bridgham, S.D., Ye, R., 2013. Organic matter mineralization and decomposition. Methods Biogeochem. Wetl. 385–406.

Chambers, L.G., Osborne, T.Z., Reddy, K.R., 2013. Effect of salinity pulsing events on soil organic carbon loss across an intertidal wetland gradient: a laboratory experiment. Biogeochemistry 115, 363–383. https://doi.org/10.1007/s10533-013-9841-5.

Chambers, L.G., Reddy, K.R., Osborne, T.Z., 2011. Short-term response of carbon cycling to salinity pulses in a freshwater wetland. Soil Sci. Soc. Am. J. 75. https://doi.org/10.2136/sssaj2011.0026.

Coble, P.G., 1996. Characterization of marine and terrestrial DOM in seawater using excitation-emission matrix spectroscopy. Mar. Chem. 51, 325–346. https://doi.org/10.1016/0304-4203(95)00062-3.

Cook, R.L., Birdwell, J.E., Lattao, C., Lowry, M., 2009. A multi-method comparison of Atchafalaya Basin surface water organic matter samples. J. Environ. Qual. 38, 702–711.

Couvillion, B.R., Beck, Holly, Schoolmaster, Donald, Fischer, Michelle, 2017. Land area change in coastal Louisiana 1932 to 2016: U.S. Geological Survey Scientific Investigations Map 3381, 16 p. pamphlet, https://doi.org/10.3133/sim3381.

Cory, R.M., McKnight, D.M., 2005. Fluorescence spectroscopy reveals ubiquitous presence of oxidized and reduced quinones in dissolved organic matter. Environ. Sci. Technol. 39, 8142–8149. https://doi.org/10.1021/es0506962.

Dagg, M.J., Ammerman, J.W., Amon, R.M.W., Gardner, W.S., Green, R.E., Lohrenz, S.E., 2007. A review of water column processes influencing hypoxia in the northern Gulf of Mexico. Estuaries Coasts 30, 735–752.

Delaune, R.D., Devai, I., Crozier, C.R., Kelle, P., 2002. Sulfate reduction in Louisiana marsh soils of varying salinities. Commun. Soil Sci. Plant Anal. 33, 79–94. https://doi.org/10.1081/CSS-120002379.

DeLaune, R.D., White, J.R., 2012. Will coastal wetlands continue to sequester carbon in response to an increase in global sea level?: a case study of the rapidly subsiding Mississippi river deltaic plain. Clim. Change 110, 297–314.

Feagin, R.A., Lozada-Bernard, S.M., Ravens, T.M., Möller, I., Yeager, K.M., Baird, A.H., 2009. Does vegetation prevent wave erosion of salt marsh edges? Proc. Natl. Acad. Sci. 106, 10109–10113.

Feijtel, T.C., DeLaune, R.D., Patrick Jr, W.H., 1985. Carbon flow in coastal Louisiana. Mar. Ecol. Prog. Ser. Oldend. 24, 255–260.

Fellman, J.B., Hood, E., Spencer, R.G.M., 2010. Fluorescence spectroscopy opens new windows into dissolved organic matter dynamics in freshwater ecosystems: A review. Limnol. Oceanogr. 55, 2452–2462.

Francalanci, S., Bendoni, M., Rinaldi, M., Solari, L., 2013. Ecomorphodynamic evolution of salt marshes: Experimental observations of bank retreat processes. Geomorphology 195, 53–65.

Georgiou, I.Y., FitzGerald, D.M., Stone, G.W., 2005. The impact of physical processes along the Louisiana coast. J. Coast. Res. 72–89.

Ghisaidoobe, Amar B.T., Chung, Sang J., 2014. Intrinsic tryptophan fluorescence in the detection and analysis of proteins: a focus on Förster resonance energy transfer techniques. Int. J. Mol. Sci. 15 (12), 22518–22538.

Haywood, B.J., Hayes, M.P., White, J.R., Cook, R.L., 2019. Potential fate of wetland soil carbon in a deltaic coastal wetland subjected to high relative sea level rise. Sci. Total Environ., 135185.

Haywood, B.J., White, J.R., Cook, R.L., 2018. Investigation of an early season river flood pulse: Carbon cycling in a subtropical estuary. Sci. Total Environ. 635, 867–877. https://doi.org/10.1016/j.scitotenv.2018.03.379.

Ecosphere 6 (10), art206. https://doi.org/10.1890/ES14-00534.1.

Hu, Z., Wang, Z.B., Zitman, T.J., Stive, M.J.F., Bouma, T.J., 2015. Predicting long-term and short-term tidal flat morphodynamics using a dynamic equilibrium theory. J. Geophys. Res. Earth Surf. 120, 1803–1823.

Hudson, P.K., Schwarz, J., Baltrusaitis, J., Gibson, E.R., Grassian, V.H., 2007. A spectroscopic study of atmospherically relevant concentrated aqueous nitrate solutions. J. Phys. Chem. A 111, 544–548.

Jankowski, K.L., Törnqvist, T.E., Fernandes, A.M., 2017. Vulnerability of Louisiana's coastal wetlands to present-day rates of relative sea-level rise. Nat. Commun. 8, 14792.

Kolic, P.E., Roy, E.D., White, J.R., Cook, R.L., 2014. Spectroscopic measurements of estuarine dissolved organic matter dynamics during a large-scale Mississippi River flood diversion. Sci. Total Environ. 485, 518–527.

Leonardi, N., Defne, Z., Ganju, N.K., Fagherazzi, S., 2016a. Salt marsh erosion rates and boundary features in a shallow Bay. J. Geophys. Res. Earth Surf. 121, 1861–1875.

Leonardi, N., Ganju, N.K., Fagherazzi, S., 2016b. A linear relationship between wave power and erosion determines salt-marsh resilience to violent storms and hurricanes. Proc. Natl. Acad. Sci. 113, 64–68.

Lützow, M.v., Kögel-Knabner, I., Ekschmitt, K., Matzner, E., Guggenberger, G., Marschner, B., Flessa, H., 2006. Stabilization of organic matter in temperate soils: mechanisms and their relevance under different soil conditions–a review. Eur. J. Soil Sci. 57, 426–445.

Manca, E., Cáceres, I., Alsina, J.M., Stratigaki, V., Townend, I., Amos, C.L., 2012. Wave energy and wave-induced flow reduction by full-scale model Posidonia oceanica seagrass. Cont. Shelf Res. 50, 100–116.

McLoughlin, S.M., Wiberg, P.L., Safak, I., McGlathery, K.J., 2015. Rates and forcing of marsh edge erosion in a shallow coastal bay. Estuaries Coasts 38, 620–638. https://doi.org/10.1007/s12237-014-9841-2.

Möller, I., Kudella, M., Rupprecht, F., Spencer, T., Paul, M., Van Wesenbeeck, B.K., Wolters, G., Jensen, K., Bouma, T.J., Miranda-Lange, M., 2014. Wave attenuation over coastal salt marshes under storm surge conditions. Nat. Geosci. 7, 727.

Morton, R.A., Bernier, J.C., Kelso, K.W., 2009. Recent subsidence and erosion at diverse wetland sites int he southeastern Mississippi Delta Plain.

Munk, W.H., Traylor, M.A., 1947. Refraction of ocean waves: a process linking underwater topography to beach erosion. J. Geol. 55, 1–26.

Murphy, K.R., Butler, K.D., Spencer, R.G.M., Stedmon, C.A., Boehme, J.R., Aiken, G.R., 2010. Measurement of dissolved organic matter fluorescence in aquatic environments: an interlaboratory comparison. Environ. Sci. Technol. 44, 9405–9412.

Parlanti, E., Wörz, K., Geoffroy, L., Lamotte, M., 2000. Dissolved organic matter fluorescence spectroscopy as a tool to estimate biological activity in a coastal zone submitted to anthropogenic inputs. Org. Geochem. 31 (12), 1765–1781.

Rabalais, N.N., Turner, R.E., Wiseman Jr, W.J., 2002. Gulf of Mexico hypoxia, aka "The dead zone". Annu. Rev. Ecol. Syst. 33, 235–263.

Reddy, K.R., DeLaune, R.D., 2008. Biogeochemistry of Wetlands: Science and Applications. CRC Press.

Sapkota, Y., White, J.R., 2019a. Marsh edge erosion and associated carbon dynamics in coastal Louisiana: a proxy for future wetland-dominated coastlines world-wide. Estuar. Coast Shelf Sci. 106289.

Sapkota, Y., White, J.R., 2019b. Carbon offset market methodologies applicable for coastal wetland restoration and conservation in the United States: A review. Sci. Total Environ.

Schwimmer, R., 2001. Rates and processes of marsh shoreline erosion in Rehoboth Bay, Delaware, USA. J. Coast. Res. 17, 672–683. https://doi.org/10.2307/4300218.

Sollins, P., Homann, P., Caldwell, B.A., 1996. Stabilization and destabilization of soil organic matter: mechanisms and controls 74, pp. 65–105.

Steinmuller, H.E., Chambers, L.G., 2018. Can saltwater intrusion accelerate nutrient export from freshwater wetland soils? An experimental approach. Soil Sci. Soc. Am. J. 82. https://doi.org/10.2136/sssaj2017.05.0162.

Steinmuller, H.E., Chambers, L.G., 2019. Characterization of coastal wetland soil organic matter: Implications for wetland submergence. Sci. Total Environ. 677, 648–659.

Steinmuller, H.E., Dittmer, K.M., White, J.R., Chambers, L.G., 2019. Understanding the fate of soil organic matter in submerging coastal wetland soils: A microcosm

approach. Geoderma 337, 1267–1277.
Tonelli, M., Fagherazzi, S., Petti, M., 2010. Modeling wave impact on salt marsh boundaries. J. Geophys. Res. Ocean 115.
Vaccare, J., Meselhe, E., White, J.R., 2019. The denitrification potential of eroding wetlands in Barataria Bay, LA, USA: Implications for river reconnection. Sci. Total Environ. 686, 529–537.
Valentine, K., Mariotti, G., 2019. Wind-driven water level fluctuations drive marsh edge erosion variability in microtidal coastal bays. Cont. Shelf Res. 176, 76–89.
van de Koppel, J., van der Wal, D., Bakker, J.P., Herman, P.M.J., 2004. Self-organization and vegetation collapse in salt marsh ecosystems. Am. Nat. 165, E1–E12.
Wang, H., van der Wal, D., Li, X., van Belzen, J., Herman, P.M.J., Hu, Z., Ge, Z., Zhang, L., Bouma, T.J., 2017. Zooming in and out: Scale dependence of extrinsic and intrinsic factors affecting salt marsh erosion. J. Geophys. Res. Earth Surf. 122, 1455–1470. https://doi.org/10.1002/2016JF004193.
Wang, Y., Zhang, D., Shen, Z., Feng, C., Chen, J., 2013. Revealing sources and distribution changes of dissolved organic matter (DOM) in pore water of sediment from the Yangtze estuary. PLoS One 8 e76633.
Weiss, R., 1974. Carbon dioxide in water and seawater: the solubility of a non-ideal gas. Mar. Chem. 2, 203–215.
White, E., Messina, F., Moss, L., Meselhe, E., 2018. Salinity and marine mammal dynamics in barataria basin: historic patterns and modeled diversion scenarios. Water 10, 1015.
White, J.R., Reddy, K.R., 2000. The effects of phosphorus loading on organic nitrogen mineralization of soils and detrius along a nutrient gradient in the northern Everglades, Florida. SSSAJ 65, 1525–1534.
Yang, S.L., Shi, B.W., Bouma, T.J., Ysebaert, T., Luo, X.X., 2012. Wave attenuation at a salt marsh margin: a case study of an exposed coast on the Yangtze Estuary. Estuaries Coasts 35, 169–182.